# Synthesis, electronic and photophysical investigations of ruthenium-centred heterometallic Kuratowski complexes which feature redox-active metal centres

**Wiebke G. Rehfuß, Andreas Kalytta-Mewes, Maryana Kraft, Binh Minh Nguyen, Wolfgang Brütting, Dirk Volkmer**

**Angaben zur Veröffentlichung / Publication details:**

Rehfuß, Wiebke G., Andreas Kalytta-Mewes, Maryana Kraft, Binh Minh Nguyen, Wolfgang Brütting, and Dirk Volkmer. 2025. "Synthesis, electronic and photophysical investigations of ruthenium-centred heterometallic Kuratowski complexes which feature redox-active metal centres." *Dalton Transactions* 54 (17): 6910–21. https://doi.org/10.1039/d5dt00088b.



# Synthesis, electronic and photophysical investigations of ruthenium(II)-centred heterometallic Kuratowski complexes which feature redox-active metal centres†

Wiebke G. Rehfuß,[a] Andreas Kalytta-Mewes,[a] Maryana Kraft,[a] Binh Minh Nguyen,[b] Wolfgang Brütting[b] and Dirk Volkmer *[a]

We present the synthesis and comprehensive characterization of a series of complexes belonging to the Kuratowski ($K_{3,3}$) family. These are pentanuclear {$Ru^{II}M_4$} complexes (M = $Co^{2+}$, $Ni^{2+}$, $Zn^{2+}$) which were prepared by employing a directed two-step synthesis facilitated by the recently published [$Ru^{II}(Me_2bta)_2(Me_2btaH)_4$] precursor complex ($Me_2$btaH = 5,6-dimethyl-1,2,3-benzotriazole). The pentanuclear Kuratowski complexes showcase a unique combination of photo-active ruthenium with redox-active metal centres. The $\mu_3$-bridging 1,2,3-triazolate ligands in these complexes facilitate electronic coupling between the metal centers, as revealed through electrochemical and photophysical studies. Comparisons with {$Ru^{II}Zn_4$} and {$Ru^{II}Cu_4$} Kuratowski compounds reveal that Co(II) significantly influences both the Ru(II/III) redox step and the position of the MLCT (metal-to-ligand charge transfer) band, whereas Cu(II) and Ni(II) exhibit minimal influence. Photophysical investigations reveal the {$Ru^{II}Zn_4$} compound as the only phosphorescent species, displaying an emission band extending into the near-infrared region. This emission originates from a triplet $^3$MLCT state and features an exceptionally large Stokes shift, with a long lifetime of the excited-state of about 3.3 μs in powdered form at room temperature.

## Introduction

In recent decades, $d^6$-metal complexes featuring nitrogen-donor ligands have been extensively explored for their photophysical and electrochemical properties.[1–7] These compounds, known for their long-lived excited states, have attracted attention due to their potential in electron transfer processes and within the expansive domain of photocatalytic applications.[8–13] We turned the scope of our investigation towards ruthenium complexes featuring 1,2,3-triazole ligands.[14–18] 1,2,3-Triazole complexes offer the distinct potential of engaging in the formation of versatile multimetallic coordination structures with transition metal ions.[19–21] One unique multimetallic coordination unit consisting of 1,2,3-triazole ligands is the Kuratowski complex which we have described in a series of publications.[22–24] These complexes consist of one central metal ion which is coordinated by the central ($N^2$) nitrogen of six 1,2,3-triazolates. This creates four peripheral coordination sites in which the metal ions are each coordinated by three external ($N^1$ or $N^3$) nitrogen atoms of the $\mu_3$-bridging 1,2,3-triazolates. The peripheral metal centres' coordination environment is finalized by an anionic side ligand, which can adopt various coordination modes. The bond topology of these highly symmetric complexes is characterized by the rare nonplanar $K_{3,3}$ graph, first described by the mathematician Kuratowski in 1930.[25]

In 2011, we reported the synthesis of the first ruthenium(II)-centred Kuratowski complex. This complex was obtained by reaction of an unidentified precursor, tentatively designated as $[Ru^{II}(Me_2btaH)_6]Cl_2$ ($Me_2$btaH = 5,6-dimethyl-1,2,3-benzotriazole), with zinc(II) chloride, resulting in the formation of $[Ru^{II}Zn_4Cl_4(Me_2bta)_6]$.[26] Powder samples of this complex show a long-lived excited state of about $\tau$ =17.4 μs. Solid state measurements are of great interest for Kuratowski compounds as the Kuratowski unit additionally comprises the secondary building unit of a large group of metal–organic frameworks, such as MFU-4 l(arge), which has proven great catalytic applications, including olefin polymerization and activation of small molecules.[27] Therefore, the incorporation of ruthenium

[a]Institute of Physics, Chair of Solid State and Materials Science, Augsburg University, Universitätsstrasse 1, D-86159 Augsburg, Germany.
E-mail: dirk.volkmer@physik.uni-augsburg.de
[b]Institute of Physics, Chair of Experimental Physics IV, Augsburg University, Universitätsstrasse 1, 86159 Augsburg, Germany

†Electronic supplementary information (ESI) available. CCDC 2402422 and 2402426. For ESI and crystallographic data in CIF or other electronic format see DOI: https://doi.org/10.1039/d5dt00088b

(II) into these MOF structures holds significant potential for photocatalytic applications. However, the integration of ruthenium(II) into these MOFs continues to be an ongoing research objective thus far. Consequently, we have shifted our focus to ruthenium(II)-centred Kuratowski complexes to enhance our understanding of the intricate coupling of electronic states between the metal ions within these complexes. Particularly, the exploration of ruthenium(II) in combination with redox-active metal ions has been limited thus far, despite holding significant catalytic potential.[28] Most recently, we accomplished the successful characterization of $[Ru^{II}(Me_2bta)_2(Me_2btaH)_4]$, which is an ideal template for inserting transition metal ions into the peripheral coordination sites of Kuratowski complexes, as seen in Fig. 1.[29] This paper focuses on the two-step synthesis of heterometallic ruthenium-centred Kuratowski complexes featuring redox-active metal ions in the peripheral positions. The results are compared with those gleaned from $\{RuZn_4\}$ compounds.[26] In these complexes, the chloride side ligands are replaced post-synthetically with the tripodal tris(3,5-dimethyl-1-pyrazolyl) borate [Tp*] "scorpionate" ligands.[23,29,30] While this substitution significantly enhances the solubility of the complexes, its primary purpose is to stabilize a well-defined octahedral coordination geometry for the peripherally coordinated metal ions.

In this article we will provide a complete characterization of the novel Kuratowski complexes, as well as investigations on their redox and photophysical properties.

## Results and discussion

### Syntheses and characterization

In this work we report on the successful development of a multi-step synthesis for Kuratowski compounds comprising a central Ru(II) metal ion. The recently published synthesis of $[Ru^{II}(Me_2bta)_2(Me_2btaH)_4]$ enabled the further extension of Kuratowski complex chemistry, as the complex provides a topologically ideal template for the addition of peripheral metal ions, as seen in Fig. 2.

In order to synthesize a heterometallic $\{Ru^{II}Co_4\}$ compound $[Ru^{II}(Me_2bta)_2(Me_2btaH)_4]$ was deprotonated with four equivalents of 2,6-lutidine in methanol at room temperature. Addition of four equivalents $CoCl_2{\cdot}6H_2O$ in methanol results in a yellow precipitate which changes it colour to dark green upon drying. The crude product was recrystallized from bromobenzene and yielded the pentanuclear Kuratowski complex $[Ru^{II}Co_4Cl_4(Me_2bta)_6]$ (**1**) as dark green octahedral crystals with a 68% yield (Fig. 3 and S1, ESI†). Similar reaction conditions were used for the synthesis of a heterometallic $\{Ru^{II}Ni_4\}$ compound, however recrystallization from bromobenzene did not yield the expected pentanuclear Kuratowski complex. Instead, prismatic orange crystals furnished the decanuclear complex $[Ru^{II}_2Ni_8Cl_8(Me_2bta)_{12}]$ (**2**) with an 80% yield (Fig. S2, ESI†). This compound consists formally of two Kuratowski complexes, which are dimerized on one corner of the peripheral nickel centres by two nickel–chloride–nickel bridges, as seen schematically in Fig. 2. Therefore, compound **2** represents a new extension of the crystallographic entities 1,2,3-triazoles can form with metal halides.

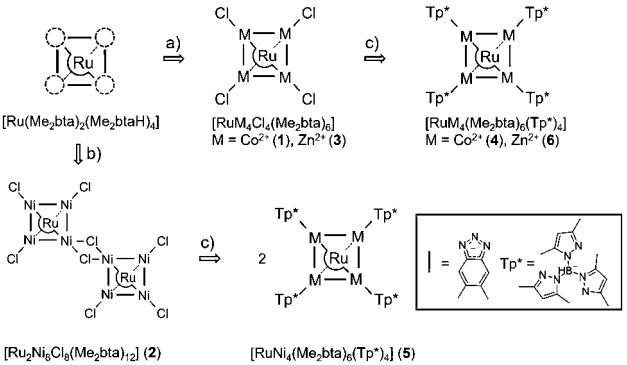


**Fig. 2** Reaction of $[Ru^{II}(Me_2bta)_2(Me_2btaH)_4]$ with (a) $MCl_2$ [M = Co(II), Zn(II)] to yield **1** and **3**; (b) $NiCl_2$ to yield **2**. (c) Subsequent ligand exchange reaction with $[NBu_4][Tp^*]$ yielding compounds **4**, **5** and **6**.

In addition, the synthesis of the previously published $[Ru^{II}Zn_4Cl_4(Me_2bta)_6]$ (**3**) complex was greatly improved employing the readily available $[Ru^{II}(Me_2bta)_2(Me_2btaH)_4]$ precursor complex. $[Ru^{II}(Me_2bta)_2(Me_2btaH)_4]$ was reacted with four equivalents of $ZnCl_2$ in dimethylformamide (DMF) at 120 °C, resulting in the formation of compound **3** in an 87% yield. This is a significant improvement on the previous synthesis, in which only a yield of 26% was achieved.[26]

Additionally, side ligand exchange of the halide ligands with tripodal capping ligands [Tp*] results in an octahedral coordination of all five metal centers.[29,30] This octahedral

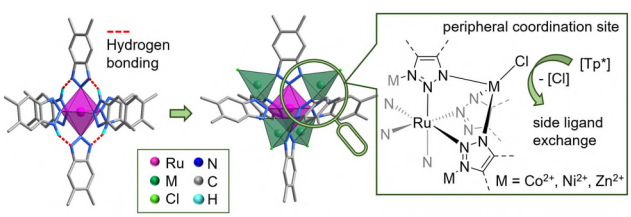


**Fig. 1** Left: Ruthenium precursor $[Ru^{II}(Me_2bta)_2(Me_2btaH)_4]$. Right: Kuratowski complex with tetrahedrally coordinated peripheral metal centres.

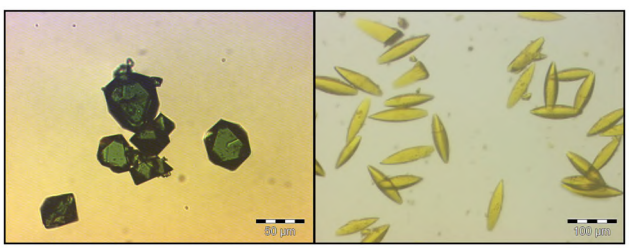

**Fig. 3** Optical microscope images of compounds **1** (left) and **4** (right).

environment promotes reversible transitions between the +II and +III oxidation states by minimizing energy differences between d-orbital levels, in contrast to their tetrahedrally coordinated counterparts. The exchange of halide ligands with [Tp*] proceeds with near-quantitative yields and prevents the formation of multiple stereoisomers, which could otherwise result from the coordination of monodentate ligands, such as those found in solvent mixtures. By reducing stereochemical complexity, the [Tp*] ligands ensure a uniform coordination environment, enabling clear and interpretable redox properties.

For the ligand exchange reaction, a DMF solution of the tetrabutyl ammonium salt of [Tp*] was added to a DMF suspension of the respective Kuratowski complex at room temperature under argon atmosphere. The product precipitates after the reaction mixture is left to stand for several days. In the case of compound **1** the addition of [Tp*] leads to a colour change from dark green to yellow and lens shaped crystals of $[Ru^{II}Co_4(Me_2bta)_6(Tp^*)_4]$ (**4**), as seen in Fig. 3 and S3, ESI.† For compound **2**, the exchange of the side ligands breaks the dimerization and leads to light brown lens shaped crystals of $[Ru^{II}Ni_4(Me_2bta)_6(Tp^*)_4]$ (**5**), (Fig. S4, ESI†). Lastly, compound $[Ru^{II}Zn_4(Me_2bta)_6(Tp^*)_4]$ (**6**) precipitated as a fine yellow crystalline powder. Prismatic single crystals can be obtained after slow evaporation of a trichloromethane solution of **6**, shown in Fig. S5, ESI.† All compounds described here are stable upon exposure to air and moisture and exhibit no degradation after several months.

The compounds were characterized by powder X-ray diffraction (PXRD), mass spectrometry, Fourier-transform infrared (FT-IR) and Raman spectroscopy, thermogravimetric analysis (TGA), and inductively coupled plasma optical emission spectroscopy (ICP-OES). Compounds **4**, **5** and **6** were additionally characterized by $^1$H NMR and elemental analysis.

First, the phase purity of all compounds was confirmed by powder X-ray diffraction, in which the experimental diffraction patterns match with the simulations generated from the single crystal data (Fig. S6–S8, ESI†). ESI-MS measurements of compounds **1** and **2** were measured in the negative mode and reveal compound **1** as $\{\mathbf{1}\cdot 2MeO^-\}$ (Fig. S17, ESI†) and compound **2** as $\{[Ru^{II}Ni_4Cl_4(Me_2bta)_6]\cdot 2MeO^-\}$ (Fig. S18, ESI†). Compounds **4**, **5** and **6** were measured in the positive mode and observed as $\mathbf{4}^+$ and $\mathbf{6}^+$ (Fig. S19 and S21 ESI†) while **5** could only be found as a fragmented molecule with two pyrazolate rings of the [Tp*] ligands missing, as shown in Fig. S20, ESI.† Additionally, $^1$H NMR spectra of compounds **4**, **5** and **6** were measured in deuterated trichloromethane. For **6** all expected proton peaks were identified in the correct ratio (Fig. S22, ESI†). Nevertheless, a significant shift of the aromatic as well as the methyl peaks is observed which matches with previous reports of $\{Zn_5(Tp^*)_4L_6\}$ Kuratowski compounds.[30] The paramagnetic relaxation enhancement effect is evident in both **4** and **5**.[31] In the case of **4**, NMR signals corresponding to the methyl groups of the [Tp*] ligand are observed within the range of −71.9 to 43.8ppm, as illustrated in Fig. 4. The identification of these signals was accomplished through a comparative analysis with the homometallic compound

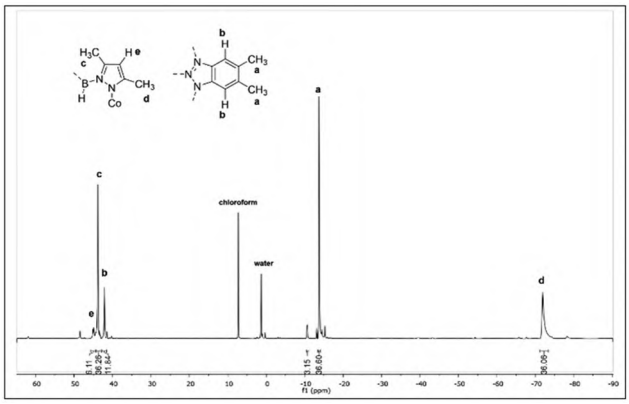


**Fig. 4** $^1$H NMR of **4** measured in deuterated trichloromethane at room temperature.

$[Co_5(Me_2bta)_6(Tp^*)_4]$.[23] Similarly, for **5**, the distinctive peaks associated with methyl groups were successfully identified, as depicted in Fig. S24, ESI.†

IR and Raman spectra were recorded for each compound, shown in Fig. S9–S16, ESI.† In the IR spectra, in addition to the vibrational bands corresponding to the aromatic and methyl bonds, the distinctive Ru–N absorption peak at 474 $cm^{-1}$ is evident. Furthermore, for compounds **4**, **5** and **6** the vibrational band observed at 2503 $cm^{-1}$ can be assigned to the B–H bond within the [Tp*] ligand, which is exemplified for compound **4** in Fig. 5.

The thermal stability of all compounds was evaluated using TGA. Compounds **1** and **2** exhibit a mass loss of 14% and 11%, respectively, at approximately 150 °C, corresponding to the loss of co-crystallized bromobenzene. The calculated mass loss for bromobenzene per formula unit is 10%, aligning well with these observations. In contrast, compounds **4**, **5**, and **6** show no detectable mass loss prior to degradation and demonstrate thermal stability up to around 400 °C. TGA curves for compounds **1** and **4** are displayed in Fig. 6, while those for the remaining compounds are provided in Fig. S25–S27, ESI.†

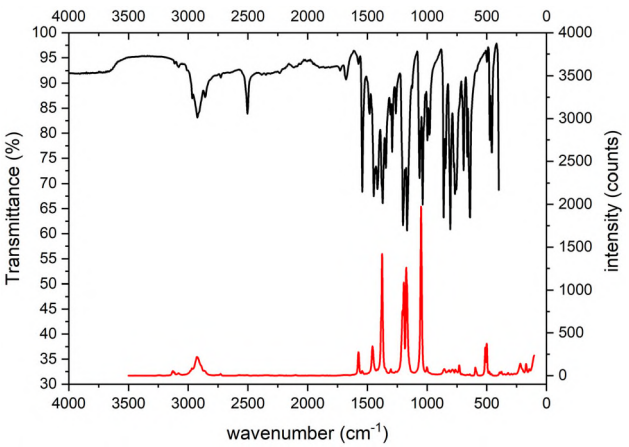


**Fig. 5** IR and Raman spectra for compound **4**.

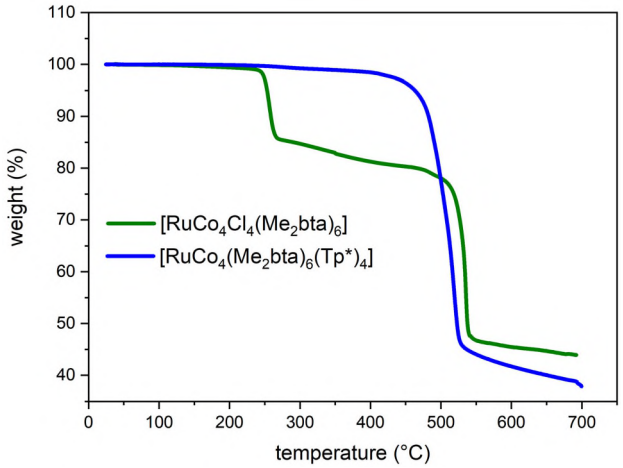


**Fig. 6** TGA curves of compounds **1** and **4**.

## Crystallographic studies

Single crystal X-ray structural analysis reveals that compound **1** crystallizes in the cubic crystal system within the highly symmetric space group $Fd\bar{3}m$ (no. 227). This structure exhibits a $T_d$-symmetric Kuratowski-type coordination unit, consistent with those previously reported for other $[M_5Cl_4(Me_2bta)_6]$ compounds.[22]

Compound **2** crystallizes in the monoclinic crystal system within space group $P2_1/c$ (no. 14). The compound formally displays two Kuratowski compounds linked through two chloride bridges between two Ni(II) centres, as shown in Fig. 7. Additionally, two co-crystallized bromobenzene molecules are found per formula unit.

The two Ru(1) centres are displaying an octahedral coordination to the central $N^2$ of six triazolate ligands whereby the bond lengths (2.073–2.087 Å) and valence angles (88.37°–92.45°; 177.59°–177.89°) are not uniform and reveal a slight distortion. There are eight peripheral Ni(II) centres in compound **2** each coordinated by three $N^1$ and $N^3$ donor atoms and with four of them being crystallographic different. Ni(2), Ni(3) and Ni(4) show a distorted tetrahedral coordination, with Ni–N bond lengths between 1.956 Å–1.977 Å. The tetrahedral coordination is completed by a chloride side ligand with bond lengths between 2.152 Å to 2.165 Å. The valence angles of the tetrahedral coordinated Ni(II) centres deviate strongly from the tetrahedral angle of 109.5°. When examining the geometry index ($\tau_4$), the values are about 0.8, which proves that geometry is similar to tetrahedral.[32] In contrast, the Ni(1) centres show a distorted square pyramidal coordination $[Ni(N_2Cl_2)_{eq}(N)_{ax}]$, as seen in Fig. 7b. The Ni(1)–N(1;9;15) bond lengths are fairly similar ranging between 1.994 Å and 2.050 Å, while the Ni(1)–Cl(1) bonds are significantly longer (2.358 and 2.410 Å). The valence angles all deviate from right (90°) angles by up to 8.49°.

Subsequently, the monodentate chloride side ligands are exchanged by tridentate [Tp*] ligands, leading to an octahedral coordination of all peripheral metal centres, as exemplified by compound **5** in Fig. 8. Hereby, the dimeric structure of compound **2** is broken. Compounds **4**, **5** and **6** are pentanuclear complexes which uniformly crystallize in the tetragonal crystal system within space group $P\bar{4}2_1/c$ (no. 114).

The side-ligand exchange introduces notable distortions in the Ru–N bond lengths of the central $RuN_6$ octahedra and reveals distinct differences in conjugation between the axial and equatorial benzotriazole ligands. In all compounds, the Ru(1)–N(4) bond exhibits slight compression relative to the Ru(1)–N(2) bond, as detailed in Table 1, with compound **6** displaying the most pronounced compression.

Interestingly, the axial benzotriazole ligands exhibit equal N–N bond lengths (N(4)–N(5)), suggesting full conjugation and delocalized electronic structures. In contrast, the equatorial benzotriazole ligands show varying N–N bond lengths (N(1)–N(2) *vs.* N(2)–N(3)), implying partial conjugation or localized electronic effects. These differences in conjugation could play a crucial role in modulating the electronic structure and excited-state properties of the complexes. Notably, these distortions are absent in compounds **1** and **3**.[26] Additionally, the N–

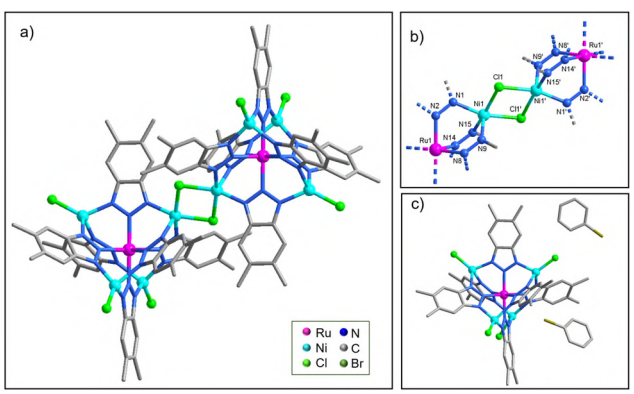


**Fig. 7** (a) Ball-and-stick representation of compound **2**. (b) Square pyramidal coordinated Ni(II) centres bridged by two chloride ligands. (c) Asymmetric unit of **2**. Hydrogen atoms are omitted for clarity.

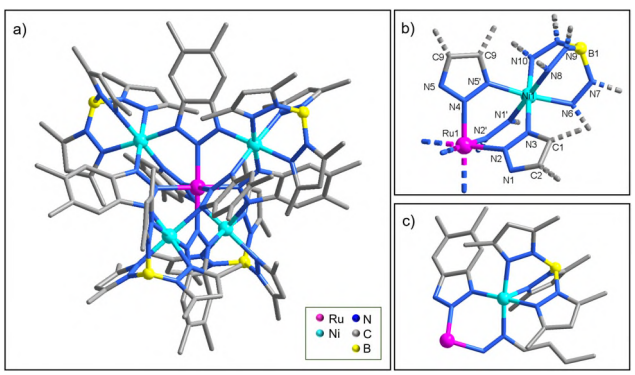


**Fig. 8** (a) Ball-and-stick representation of compound **5**. (b) Octahedral coordinated Ni(II) binding to six nitrogen, three triazolates and the tripodal [Tp*]. (c) Asymmetric unit of **5**. Hydrogen atoms are omitted for clarity.

Table 1 Selected bond lengths of compounds **4**, **5**, **6** and **7** [29]

| | 4 | 5 | 6 | 7 |
|---|---|---|---|---|
| Ru(1)–N(2) (Å) | 2.122 | 2.088 | 2.134 | 2.117 |
| Ru(1)–N(4) (Å) | 2.093 | 2.070 | 2.101 | 2.110 |
| N(1)–N(2) (Å) | 1.339 | 1.35(1) | 1.345 | 1.32(1) |
| N(2)–N(3) (Å) | 1.323 | 1.34(1) | 1.319 | 1.34(1) |
| N(4)–N(5) (Å) | 1.335 | 1.348 | 1.330 | 1.324 |

Ru–N valence angles remain close to 90° and 180° across all compounds.

For reference, selected bond lengths in $[Ru^{II}Cu_4(Me_2bta)_6(Tp^*)_4]$ (compound **7**), which was previously reported,[29] are included in Table 1 for comparative discussion of electrochemical and photophysical properties.

The peripheral metal centers exhibit diverse bond lengths, with compound **4** ranging from 2.090 to 2.179 Å, compound **5** from 2.053 to 2.14(1) Å, compound **6** from 2.114 to 2.246 Å and compound **7** from 2.031 to 2.37(1) Å. Notably, the Jahn–Teller effect of Cu(II) is evident in compound **7**, where the elongation of the axial nitrogen bond results in the largest M–N bond length of 2.37(1) Å. Additionally, similar to the Ru–N bond lengths, compound **6** exhibits longer M–N bond lengths compared to compounds **4** and **5**. This difference can be attributed to the absence of π-backbonding in Zn(II) due to its fully filled $d^{10}$ configuration. In contrast, Co(II) and Ni(II) can engage in π-backbonding, leading to shorter M–N bond lengths.

Details of the single-crystal data collection and refinement of all compounds are listed in Table S1, ESI.†

## Electrochemistry

The redox properties of compounds **4**, **5**, **6** and **7** were studied by cyclic voltammetry (CV). The voltammograms were recorded in a 0.1 M $[NBu_4][PF_6]$ trichloromethane solution and the results are summarized in Table 2. All solutions were degassed with argon and the CV data obtained at various scanning rates, are shown in Fig. S28–S32, ESI.†

Due to the poor solubility of compounds **1**, **2**, and **3**, cyclic voltammetry measurements could not be performed. Despite extensive solubility tests in solvents, including trichloromethane, acetonitrile, tetrahydrofuran, and dimethylformamide, no conditions allowed for sufficiently high concentrations required for reliable electrochemical analysis. Additionally, the halide-terminated nature of these compounds leads to ligand exchange and solvent coordination in solution, resulting in the formation of multiple species rather than a single well-defined complex.

Compound **6** displays a single-electron reversible oxidation wave ($I^{Ox}$), attributed to the Ru(II/III) redox couple, at ${}^{I}E^{ox}_{\frac{1}{2}}$ = 0.18 V *vs.* $Fc^+/Fc$ (Fig. 9, yellow). No additional redox waves were observed, consistent with the redox-inactive nature of Zn(II). Compared to the mononuclear Ru(II) compound $[Ru(bpy)_3]^{2+}$ (${}^{I}E^{ox}_{\frac{1}{2}}$ = 1.00 V *vs.* $Fc^+/Fc$[33]), the significantly lower redox potential indicates that the triazolate ligands destabilize the Ru(II) oxidation state relative to bipyridine. This is likely due to reduced π-backbonding from the Ru centre to the triazolate ligands, which is supported by the longer Ru–N bond lengths observed in the X-ray crystal structure ($[Ru(bpy)_3]^{2+}$ = 2.052 Å and 2.053 Å).

Compound **7** exhibits a similar but slightly lower redox potential at ${}^{I}E^{ox}_{\frac{1}{2}}$ = 0.15 V *vs.* $Fc^+/Fc$ (Fig. 9, purple). The incorporation of Cu(II) ions appears to render the Ru centre slightly more electron-rich. No redox waves corresponding to Cu(II) were detected within the measurement window.

Conversely, the redox potential of Ru(II) in compound **5** shifts to a slightly higher potential at ${}^{I}E^{ox}_{\frac{1}{2}}$ = 0.23 V *vs.* $Fc^+/Fc$ (Fig. 9, red). Additionally, a single-electron irreversible oxidation wave at ${}^{II}E^{ox}_{p/2}$ = 0.71 V *vs.* $Fc^+/Fc$ is observed, attributed to the Ni(II/III) redox process. Interestingly, this irreversible oxidation is only detectable in the initial scans, which are shown in Fig. S30, ESI.† A similar oxidation potential (0.59 V *vs.* $Fc^+/Fc$) has been reported for $[Ni(Tp^*)_2]$. However, the irreversible nature of the oxidation in compound **5** suggests an electrochemical reaction is taking place. This behaviour is unexpected since octahedrally coordinated Ni(III) complexes are generally very stable and are in accordance with the ligand

Table 2 Cyclic voltammetric data of compounds **4**, **5**, **6** and **7**

| Compound | ${}^{I}E^{ox}_{\frac{1}{2}}$ (${}^{I}E^{ox}_{p/2}$) | ${}^{II}E^{ox}_{p/2}$ | ${}^{I}E^{red}_{p/2}$ |
|---|---|---|---|
| **4** | 0.34 | 0.84 | −0.62 |
| **5** | 0.23 | 0.71 | |
| **6** | 0.18 | | |
| **7** | 0.15 | | |

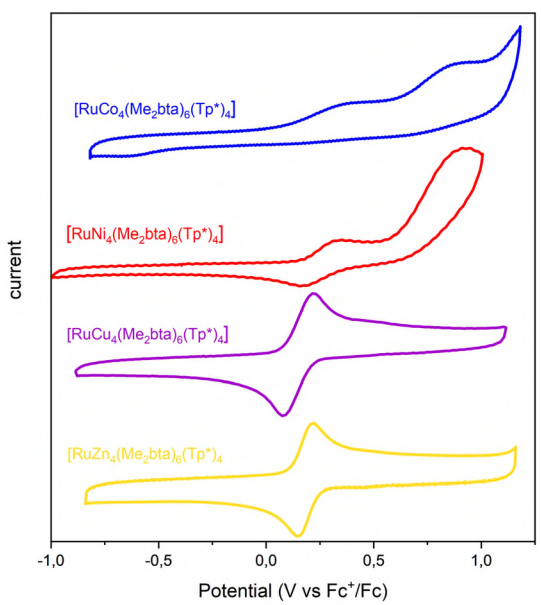


Fig. 9 Cyclic voltammograms of compounds **4**, **5**, **6** and **7** at a glassy carbon electrode in a 0.10 M $[NBu_4][PF_6]/CHCl_3$ solution, with $Ag/Ag^+$ as the reference electrode. Scan rate: 100 mV $s^{-1}$, complex concentration: 0.5 mM.

field stabilization energies. A similar irreversible oxidation has been reported for square-planar bis(bis(pyrazolyl)borate) Ni(II) complex. There, quantum chemical calculations attribute the irreversibility to charge removal from the B–H bonds, leading to proton loss and an irreversible oxidation.[34]

Compound **4** demonstrates a significant shift in the Ru(II/III) oxidation potential, observed as an irreversible single-electron oxidation wave at ${}^{I}E^{ox}_{p/2}$ = 0.34 V *vs.* $Fc^+/Fc$ (Fig. 9, blue). This represents a +0.13 V shift compared to compound **6**. Additionally, compound **4** exhibits a single-electron irreversible oxidation wave at ${}^{II}E^{ox}_{p/2}$ = 0.83 V *vs.* $Fc^+/Fc$ attributed to the Co(II/III) oxidation, and a weak single-electron irreversible reduction wave ($I^{red}$) at ${}^{I}E^{red}_{p/2}$ = −0.62 V *vs.* $Fc^+/Fc$, corresponding to the Co(II/I) reduction. The irreversibility of these redox events is surprising given the stability of Co(III) ions in an octahedral N6 coordination environment, for example in numerous published scorpionate complexes.[35,36] A potential explanation for the lack of a stable [$Ru^{III}Co^{III}$] species is the high overall charge of the pentanuclear complex, which may lead to degradation.

Furthermore, the Co(II/III) oxidation potential is higher compared to mononuclear bis(tris(pyrazolyl)borate) Co(II) complexes (−0.50 and −0.58 V *vs.* $Fc^+/Fc$).[35] However, it aligns more closely with cobalt complexes bearing C-functionalized tripodal ligands such as [$Co\{HOCH_2C(pz)_3\}_2$], which exhibit a reversible Co(II/III) oxidation at 0.58 V *vs.* $Fc^+/Fc$ and an irreversible Co(II/I) reduction at −0.68 V *vs.* $Fc^+/Fc$.[36]

In summary, the redox behaviour of these first [$Ru^{II}M^{II}_4$] Kuratowski complexes is unexpected. The octahedral coordination of the peripheral 3d M(II) ions does not sufficiently stabilize the M(III) oxidation states, resulting in irreversible processes. To improve redox stability, future synthetic efforts should focus on replacing the fragile boron-hydride bonds with boron-alkyl or boron-aryl counterparts, potentially enhancing the robustness of these heterometallic Kuratowski complexes.

## Photophysical properties

UV-Vis spectra of compounds **1** and **2** were recorded in ethanol solution. Compound **2** exhibits two distinct absorption bands at 345 nm and 275 nm, as shown in Fig. 10. The band at 275 nm is attributed to the π → π* transition (ligand-to-ligand charge transfer; LLCT) of the [$Me_2$bta] ligand, as it undergoes only a minor shift compared to the free $Me_2$btaH ligand. The band at 345 nm is assigned to a metal-to-ligand charge transfer (MLCT), consistent with previously reported data for Ru(II)-benzotriazolate complexes.[17,26,37]

The LLCT and MLCT bands of compound **2** closely resemble the absorption features of compound **3**, which were measured in an earlier study.[26] Interestingly, the MLCT band of Ru(II)-benzotriazolate complexes appears at significantly higher energies than that of $[Ru(bpy)_3]^{2+}$ complexes.[38] This observation suggests that benzotriazolate ligands have a significantly higher π* energy level compared to bipyridine ligands. Additionally, the extinction coefficient of the MLCT band is notably higher than that of the LLCT band. While this behaviour is somewhat atypical, it has been consistently observed in our measurements.

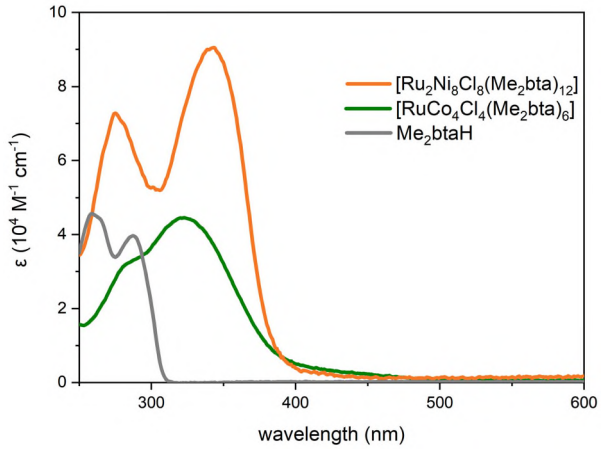


**Fig. 10** UV-vis absorption spectra of compounds **1**, **2** and $Me_2$btaH recorded in ethanol solution at room temperature.

For compound **1**, a single absorption band is observed at 320 nm, with a shoulder at 282 nm, as illustrated in Fig. 10. The inclusion of Co(II) ions appears to influence the MLCT band position, causing a noticeable blue shift of approximately 25 nm. This shift suggests that the incorporation of Co(II) ions significantly increases the HOMO–LUMO energy gap in the Ru(II)-benzotriazolate system, in comparison to {$Ru^{II}Zn_4$}, {$Ru^{II}Cu_4$} and {$Ru^{II}Ni_4$} compounds.

The fully octahedrally coordinated compounds **4**, **5**, **6** and **7** were measured in trichloromethane and are depicted in Fig. 11. Generally, the absorption bands differ only slightly from those with chloride side ligands, which is due to the fact that the intensity-weak d–d transitions cannot be observed in such highly diluted solutions. Compounds **5**, **6** and **7** show two distinct absorption bands at 283 nm and 347 nm, which are assigned to the LLCT of [$Me_2$bta] and MLCT, respectively.

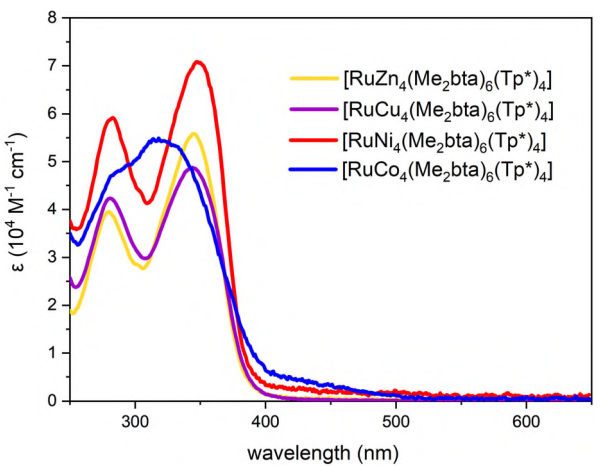


**Fig. 11** UV-vis absorption spectra of compounds **4**, **5**, **6** and **7** recorded in trichloromethane solution at room temperature.

Compound **4** shows a broad MLCT band at 312 nm with a shoulder around 283 nm. Again, the MLCT band of the $\{Ru^{II}Co_4\}$ compound is blue shifted by approximately 35 nm in comparison with the $\{Ru^{II}Zn_4\}$, $\{Ru^{II}Cu_4\}$ and $\{Ru^{II}Ni_4\}$ compounds. The molar absorption coefficient is largest for compound **5** with 70 780 $M^{-1}$ $cm^{-1}$, whereas compounds **4** and **6** exhibit very similar values of 54 900 $M^{-1}$ $cm^{-1}$ and 55 800 $M^{-1}$ $cm^{-1}$ respectively. Additionally, **7** displays a slightly lower value of 48 700 $M^{-1}$ $cm^{-1}$. Concentration-dependent UV-Vis spectra are shown in Fig. S27–S32, ESI.†

To investigate the positions of the d–d transitions, powder UV-Vis measurements of compounds **4** and **5** were recorded in Kubelka–Munk units and are shown in Fig. S33 and S34, ESI.† Compound **4** exhibits three spin-allowed transitions at 930 nm, 570 nm, and 460 nm, corresponding to the $^4T_{1g} \rightarrow {}^4T_{2g}(F)$, $^4T_{1g} \rightarrow {}^4T_{1g}(P)$ and $^4T_{1g} \rightarrow {}^4A_{2g}$ transitions, respectively. The estimated crystal field splitting parameter $D_q$ is 11 550 $cm^{-1}$, and the Racah parameter ($B$) is 543 $cm^{-1}$, which are typical for octahedrally coordinated Co(II).[39]

For compound **5**, additional absorption bands are observed at 1360 nm, 820 nm and 550 nm, corresponding to the spin-allowed $^3A_{2g} \rightarrow {}^3T_{2g}(F)$, $^3A_{2g} \rightarrow {}^3T_{1g}(F)$ and $^3A_{2g} \rightarrow {}^3T_{1g}(P)$ transitions. The estimated values for $D_q$ and $B$ are 7260 $cm^{-1}$ and 968 $cm^{-1}$, respectively.

Steady state measurements were performed in oxygen free trichloromethane solution. The emission properties of the compounds were compared to those of the $Me_2$btaH ligand and the previously reported $[RuZn_4Cl_4(Me_2bta)_2]_6$ (compound **3**).[26] Notably, the scorpionate ligand [Tp*] does not display any emission.

All four compounds show similar excitation and emission spectra. Both the excitation and emission bands are blue shifted in comparison with free $Me_2$btaH ligand, as seen in Fig. 12.

Upon excitation at 263 nm, the emission of the LLCT band is detected at approximately 315 nm for compounds **4**, **5**, **6** and **7**. The excitation of the MLCT band does not yield measurable fluorescence signals at room temperature. This phenomenon has been documented for compound **3** as well as for other ruthenium-triazolate complexes, likely attributed to the presence of low-energy $^3$MC states that are readily accessible from $^3$MLCT states through thermal processes.[18] The peak positions are summarized in Table 3.

All samples exhibit only weak fluorescence. To quantify, their quantum yields were measured and compared to standard anthracene, with a quantum yield of 33%, as shown in Fig. S35 and S36, ESI.† Compound **6** has a quantum yield of 1.3%, which is further reduced by the addition of the fluorescence quenching Co(II), Ni(II) and Cu(II) ions, with compounds **4**, **5** and **7** exhibiting quantum yields of only approx. 0.1%.

The excited lifetimes were measured using a pulsed 272 nm LASER as the excitation light source. Here, **6** shows the longest fluorescence lifetime with approx. 10 ns, while compounds **4**, **5** and **7** exhibit lifetimes of 1.3–2.4 ns, as seen in Fig. 13. The lifetime results are shown in Table 4.

Additionally, the solid-state emission properties of compounds **4**, **5**, **6**, and **7** were investigated. This study was inspired by previous observations for compound **3**, which exhibits a microsecond-long excited-state lifetime in its powdered form.[26] For compound **3**, excitation of the LLCT band at 275 nm resulted in distinct emissions at 317 nm, 415 nm, and 440 nm. These emissions suggest that excitation of the LLCT

**Table 3** Excitation and emission bands of compounds **4**, **5**, **6**, **7** and $Me_2$btaH in trichloromethane

| Compound | $\lambda_{max,exc.}$/nm | $\lambda_{wing,exc.}$/nm | $\lambda_{max,em.}$/nm | QY/% |
|---|---|---|---|---|
| **4** | 263 | 287 | 316 | 0.1 |
| **5** | 264 | | 317 | 0.1 |
| **6** | 263 | | 316 | 1.3 |
| **7** | 264 | 285 | 316 | 0.1 |
| $Me_2$btaH | 279 | | 343 | 1.9 (ref. 26) |

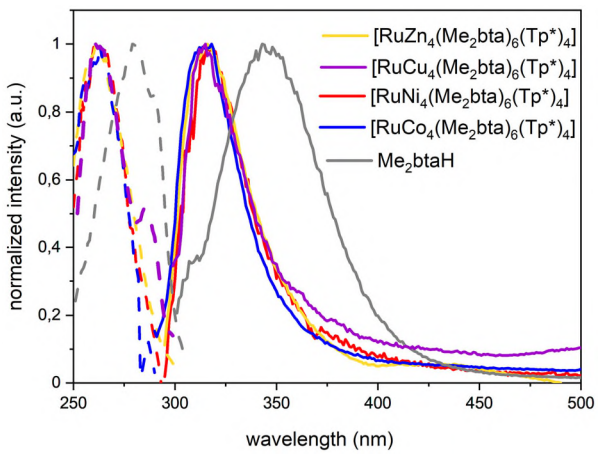


**Fig. 12** Fluorescence excitation (···) and emission (–) spectra of compounds **4**, **5**, **6**, **7** and $Me_2$btaH recorded in trichloromethane solution at room temperature.

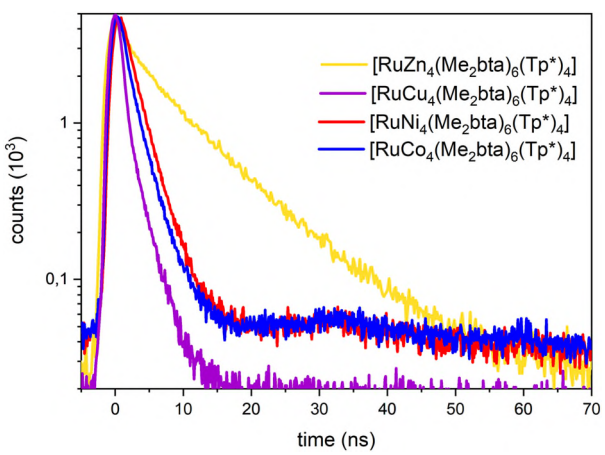


**Fig. 13** Lifetime measurements of compounds **4**, **5**, **6** and **7** recorded in trichloromethane solution at room temperature.

Table 4 Lifetimes of compounds **4**, **5**, **6** and **7**

| Compound | $\tau 1$/ns | $a1$/% | $\tau 2$/ns | $a2$/% | $X^2$ |
|---|---|---|---|---|---|
| **4** | 2.07 | 100 | | | 0.997 |
| **5** | 2.43 | 100 | | | 0.999 |
| **6** | 3.16 | 18 | 10.52 | 82 | 0.999 |
| **7** | 1.37 | 100 | | | 0.999 |
| **6** (solid state) | 3300 | 100 | | | 0.999 |

band triggers multiple photophysical processes. Specifically, the excited LLCT state appears to convert into the singlet MLCT state, which then undergoes intersystem crossing (ISC) to the triplet MLCT state. This sequential mechanism explains both the low quantum yield and extended excited-state lifetime observed for compound **3**.[26]

Among compounds **4**, **5**, **6**, and **7**, emission quenching by open-shell 3d metal ions was evident in compounds **4**, **5**, and **7**, as their emissions were too weak to detect. In contrast, compound **6** displayed markedly different behaviour compared to its solution-phase properties and compound **3**, as shown in Fig. 14.

When exciting the powdered sample of **6** at 280 nm, no significant emission corresponding to the MLCT state was detected. However, excitation of the MLCT band produced a broad red emission with a maximum in the NIR region, at approximately 810 nm. The excitation spectrum, monitored at 810 nm, showed a distinct band at 380 nm along with a broad UV profile, confirming that the emission originates from the population of the singlet MLCT state.

This corresponds to a substantial Stokes shift of 430 nm. The lifetime of the emission in the powdered sample was measured to be 3.3 μs, as shown in Fig. 15, proving its triplet MLCT state nature.

The appearance of phosphorescence from a Ru(II) complex in the far-red region is unusual, as benzotriazolate ligands are typically associated with high-lying excited states, as shown in the UV-Vis spectra.[17] The significantly lower energy of the

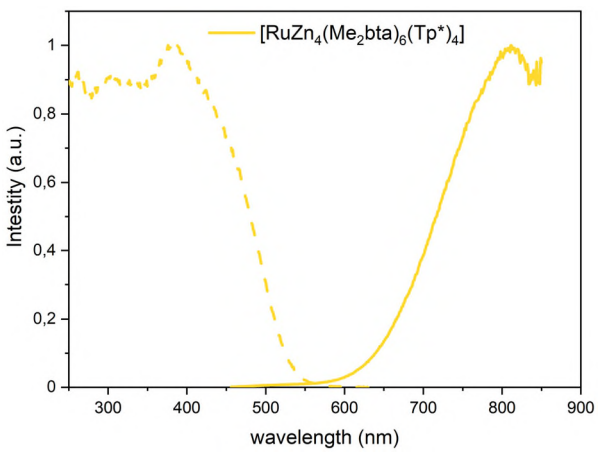


Fig. 14 Fluorescence excitation (···) and emission (–) spectra of compound **6** in solid state at room temperature.

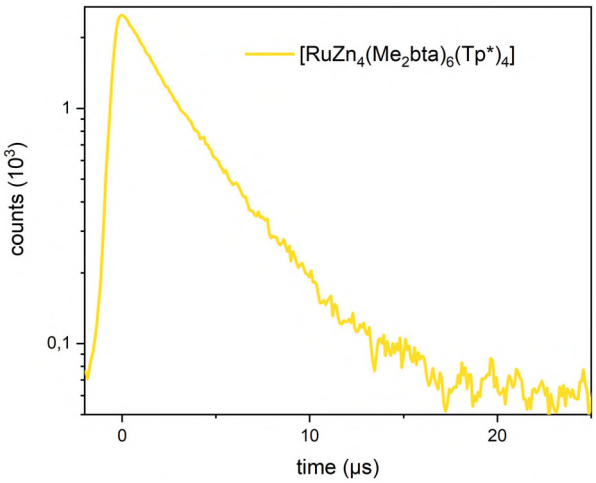


Fig. 15 Lifetime measurements of compound **6** recorded in solid state at room temperature.

emitting triplet MLCT state in this case can be attributed to significant distortion in the excited state. As discussed, the crystal structure analysis reveals notable compression of the axial benzotriazolate ligands, with conjugation differences between axial and equatorial ligands reflected in varying N–N bond lengths. These distortions create electronic asymmetry within the complex, leading to stabilization of the excited-state orbitals.[40]

Upon excitation to the MLCT state, the system likely redistributes electron density preferentially to the more conjugated axial ligands, which are better at delocalizing charge. This redistribution could result in significant geometry changes, further stabilizing the triplet MLCT state relative to the singlet state and increasing the energy gap between the ground and excited states.[41]

Additionally, the rigidity of the Kuratowski complex, with its twisted $\mu_3$-bridged benzotriazolate ligands might also play a role by restricting non-radiative decay pathways and enhancing phosphorescence from the triplet state. This rigidity, combined with the distortions and differences in ligand conjugation, provides a plausible explanation for the unusually low energy of the emitting state in compound **6**.

## Conclusion

The recently characterized ruthenium precursor complex $[Ru^{II}(Me_2bta)_2(Me_2btaH)_4]$ allowed us to synthesize and fully characterize five complexes within the Kuratowski family with Co(II), Ni(II) and Zn(II) ions located on the peripheral coordination sites. The combined photophysical and electrochemical studies of the $[Ru^{II}M_4(Me_2bta)_6(Tp^*)_4]$ (M = $Co^{II}$, $Ni^{II}$, $Cu^{II}$ and $Zn^{II}$) complexes provide valuable insights into their structural and functional properties. The fluorescence and phosphorescence behaviour, particularly in solid-state measurements, highlight the sensitivity of the triplet MLCT state to both struc-

tural and electronic factors. Compound **6** demonstrated a unique emission profile with a broad, red-shifted phosphorescence and a significant Stokes shift, attributed to axial ligand compression and differences in conjugation between axial and equatorial benzotriazole ligands. These findings emphasize the importance of the octahedral coordination around the peripheral metal ions in controlling these effects. Moreover, avoiding 3d open-shell metal ions helps minimize quenching effects, preserving long-lived triplet states essential for potential photophysical applications. Electrochemical studies revealed that the Ru(II)/Ru(III) redox potential remains remarkably stable, even in the presence of quenching 3d metal ions such as Ni(II) and Cu(II). However, Co(II) significantly affects both the reversibility and the redox potential of the Ru(II)/Ru(III) couple, indicating a stronger electronic interaction with the Ru centre. While the complexes demonstrated stability as {Ru(III)M(II)$_4$} assemblies, no other stable mixed-valent variants were identified, limiting their potential for multi-electron transfer processes. To explore catalytic applications, *e.g.* for small molecule reductions, it would be essential to develop Kuratowski-type complexes with higher metal-centred electron mobility. Future work could focus on incorporating early transition metal ions such as V(II) or Fe(II), which are strong reducing agents, to enhance the electronic versatility of these systems.

# Experimental

### Materials and methods

All chemicals were purchased from commercial suppliers in reagent grade and used without further purification unless otherwise mentioned. [NBu$_4$][Tp*] was obtained *via* metathesis reaction of tetrabutylammonium chloride and commercially available [Tp*] potassium salt in dry THF, similar to literature procedures.[23] Fourier transform infrared (FT-IR) spectra were recorded with an ATR unit in the range of 4000–400 cm$^{-1}$ on a Bruker Equinox 55 FT-IR spectrometer and were labelled s (strong), m (medium), and w (weak) to assign signal intensities. Raman spectra were recorded with a Thermo Scientific DXR Raman Microscope equipped with a laser excitation at 532 nm. The spectra were acquired in the 3500–100 cm$^{-1}$ spectral range. Molecular masses were measured with a Q-Tof Ultima mass spectrometer (Micromass) equipped with an ESI source. Mass spectra were calibrated using phosphoric acid. Thermogravimetric analysis (TGA) data was collected with a TA Instruments Q500 device in the temperature range of 25–700 °C in flowing nitrogen gas at the heating rate of 10 K min$^{-1}$. $^1$H NMR spectra were recorded in deuterated chloroform solutions with a Mercury plus 400 high-resolution system (Variant Deutschland GmbH). ESEM micrographs were recorded with a Philips XL 30 scanning electron microscope. ICP-OES analysis were performed on a Vista MPX of VARIAN with ruthenium standard solutions of 10 ppm and cobalt, nickel and zinc standard solutions of 20 ppm. Elemental analysis was performed with a Vario EL III instrument (Elementar-Analysensysteme GmbH). Powder X-ray diffraction patterns (PXRD) were collected at room temperature in the range of 4°–50° 2$\theta$ with a Seifert XRD 3003 TT powder diffractometer with a Meteor1D detector and Cu Kα1 radiation. The cyclic voltammograms were recorded on a biologic SP-300 potentiostat using a three-electrode system (glassy carbon working electrode, 3 mm in a diameter, a pseudo reference electrode and a platinum wire counter electrode). The experiments were carried out at room temperature at different scan rates from 200 to 10 mV s$^{-1}$ in water and oxygen free trichloromethane solutions under argon atmosphere. UV–vis spectra were recorded in the range of 1600–250 nm on a PerkinElmer λ 750s spectrometer with dual-beam. Fluorescence measurements were performed on an Edinburgh instruments FLS920 equipped with double monochromators in excitation and emission light path, a TE Cooled R928P PMT detector and a Xe900 continous xenon lamp. For fluorescence life time measurements, a picosecond pulsed LED with an excitation wavelength of 272 nm was used. All measurements were done at room temperature in standard quartz glass cuvettes with a 10 mm pathlegth. All samples (except the standard sample anthracene) were dissolved in stabilizer-free chloroform spectroscopic grade (Uvasol®) in the given concentrations, as well as homogenized and degassed. Solid-state fluorescence measurements were performed on the same instrument with a quartz glass powder sample holder. Solid-state fluorescence life time was measured by excitation with a EKSPLA PT400 pulsed laser and recorded by a Hamamatsu C5680 streak camera combined with a Acton Spectra Pro 2300i, Princeton Instruments spectrograph.

### Single crystal X ray diffraction

Single crystal X-ray diffraction measurements were conducted by picking crystals directly from the mother liquor and collecting the X-ray reflection data using a Bruker D8 Venture diffractometer equipped by a low temperature device. Intensity measurements were performed using monochromated (doubly curved silicon crystal) MoKα radiation (0.71073 Å) from a sealed microfocus tube. The raw data frames were integrated and corrected for absorption effects using the Bruker SAINT (Bruker, 2019. Apex3 v2019.1-0, SAINT V8.40A, Bruker AXS Inc.: Madison (WI), USA.) and SADABS software packages.[42] Structure solution by direct methods and structure refinement were performed using SHELXT 2014/5 [43] and SHELXL 2018/3.[44] All non-hydrogen atoms were refined anisotropically. All hydrogen atoms of the compounds were positioned geometrically and constrained to ride on their parent atoms. The crystallographic data for the structures reported in this paper are presented in Table S1, ESI.† Complete crystallographic data can be obtained from the Cambridge Crystallographic Data Centre as supplementary publication no. CCDC 2402422–2402426.†

**[RuCo$_4$Cl$_4$(Me$_2$bta)$_6$] (1).** A solution of CoCl$_2$·6H$_2$O (95 mg, 0.40 mmol) in MeOH (1.6 mL) was slowly added to a suspension of [Ru(Me$_2$bta)$_2$(Me$_2$btaH)$_4$] (100 mg, 0.10 mmol) and 2,6-lutidine (46 μL, 0.40 mmol) in MeOH (1.6 mL) and stirred at rt for 2 d. The resulting yellow solid was filtered and dried whereby the colour changed to dark green. The crude product

was then recrystallized from bromobenzene (8.0 mL) to yield **1** as green octahedral crystals (97 mg, 0.06 mmol, 68%).

IR (ATR, 4000–400 $cm^{-1}$): 3050 (w), 2981 (m), 2946 (w), 2898 (w), 2861 (w), 1643 (w), 1577 (m), 1488 (m), 1473 (w), 1643 (w), 1577 (m), 1488 (m), 1473 (m), 1454 (s), 1388 (w), 1375 (m), 1309 (m), 1189 (s), 1164 (m), 1068 (m), 1027 (m), 1189 (s), 1164 (m), 1068 (m), 1027 (m), 1000 (s), 971 (w), 852 (s), 836 (m), 794 (w), 754 (s), 734 (m), 721 (w), 690 (m), 673 (m), 582 (w), 501 (w), 480 (s), 468 (m), 441 (w).

Raman ($cm^{-1}$): 3052 (w), 2948 (w), 2905 (w), 1574 (m), 1458 (m), 1377 (s), 1310 (w), 1193 (s), 1164 (s), 1067 (s), 998 (w), 849 (w), 721 (m), 582 (w), 507 (m), 480 (w), 404 (w), 373 (w), 260 (w), 193 (w), 168 (m), 143 (s), 113 (m). ESI-MS (*m*/*z*) for $[RuCo_4C_{50}N_{18}H_{54}Cl_4O_2]^-$: 1416.97 (calc.); 1416.91 (found).

ICP-OES Ru/Co ratio expected 1 : 4; measured 1 : 4.08.

**$[Ru_2Ni_8Cl_8(Me_2bta)_{12}]$ (2).** A solution of $NiCl_2{\cdot}6H_2O$ (95 mg, 0.40 mmol) in acetone (15 mL) was slowly added to a suspension of $[Ru(Me_2bta)_2(Me_2btaH)_4]$ (100 mg, 0.10 mmol) and 2,6-lutidine (46 μL, 0.40 mmol) in EtOH (3.0 mL) and stirred at rt for 2 d. The orange solution was concentrated *in vacuo*. The residue was recrystallized from bromobenzene (5 mL) and washed with water to yield **2** as orange prismatic crystals (115 mg, 0.04 mmol, 80%).

IR ($cm^{-1}$): 3316 (w), 3056 (w), 2975 (w), 2900 (w), 2435 (s), 2051 (w), 1980 (w), 1722 (m), 1635 (s), 1575 (s), 1462 (s), 1442 (s), 1405 (s), 1384 (s), 1311 (s), 1295 (s), 1259 (w), 1201 (s), 1068 (s), 1020 (s), 998 (s), 916 (w), 852 (s), 831 (s), 802 (s), 736 (s), 715 (m), 688 (m), 682 (s), 671 (s), 588 (w), 555 (s), 509 (w), 484 (s), 457 (m9), 420 (s).

Raman ($cm^{-1}$): 3069 (w), 2926 (w), 1622 (w), 1570 (s), 1456 (s), 1372 (s), 1303 (m), 1261 (w), 1206 (s), 1173 (s), 1068 (s), 997 (w), 852 (w), 832 (w), 726 (m), 695 (w), 586, (w), 507 (s), 482 (w), 371 (w), 192 (w), 131 (w). ESI-MS (*m*/*z*) for $[RuNi_4C_{50}N_{18}H_{54}Cl_4O_2]^-$: 1414.98 (calc.); 1414.96 (found).

ICP-OES Ru/Ni ratio expected 1 : 4; measured 1 : 3.93.

**$[RuZn_4Cl_4(Me_2bta)_6]$ (1).** The synthesis of $[RuZn_4Cl_4(Me_2bta)_6]$ has been previously reported.[26] While the experimental conditions remain consistent, we obtained a higher yield due to the due to the use of $[Ru(Me_2bta)_2(Me_2btaH)_4]$, which was characterized more recently.[29]

A suspension of $[Ru(Me_2bta)_2(Me_2btaH)_4]$ (100 mg, 0.10 mmol) was dissolved in 12 mL DMF and heated to 100 °C until fully dissolved, then $ZnCl_2$ (55 mg, 0.40 mmol) was added and the solution was heated to 120 °C in a closed vessel. After holding this temperature for 2 h, the mixture was cooled to room temperature and yellow octahedral crystals were collected by filtration, washed with 2 × 5 mL DMF and vacuum dried. Yield: 134 mg, 0.09 mmol 87%.

IR ($cm^{-1}$): 3050 (w), 2979 (w), 2946 (w), 2898 (w), 2861 (w), 2782 (w), 21 710 (w), 1644 (w), 1623 (w), 1577 (m), 1488 (w), 1452 (s), 1390 (w), 1375 (m), 1311 (m), 1255 (w), 1189 (vs), 1160 (m), 1070 (m), 1027 (m), 1000 (vs), 975 (w), 852 (vs), 842 (m), 796 (w), 754 (vs), 732 (w), 690 (m), 673 (m), 582 (m), 480 (m), 468 (m), 404 (s).

**$[RuCo_4(Me_2bta)_6(Tp^*)_4]$ (4).** A solution of $[NBu_4][Tp^*]$ (80 mg, 0.15 mmol) in degassed DMF (1.5 mL) was added dropwise to a solution of **1** (50 mg, 0.03 mmol) in degassed DMF (1.5 mL) under argon atmosphere. The solution was stirred at rt for 2 h while the colour changed from dark green to yellow. The mixture was allowed to stand for 5 d, after which the precipitate was filtered and washed with methanol. The product was dissolved in trichloromethane and additionally filtered over a short column of basic aluminum oxide. Slow evaporation of the solvent yields **4** as a yellow crystalline product (73 mg, 0.03 mmol, 93%).

IR ($cm^{-1}$): 3307 (w), 3126 (w), 3087 (w), 2962 (m), 2923 (s), 2865 (m), 2726 (w), 2508 (m), 2445 (w), 2335 (w), 1724 (w), 1544 (s), 1481 (m), 1444 (s), 1415 (s), 1376 (s), 1355 (s), 1307 (w), 1292 (m), 1259 (m), 1205 (s), 1184 (s), 1101 (s), 1062 (s), 1043 (s), 998 (s), 858 (s), 809 (s), 775 (s), 723 (m), 694 (s), 653 (m), 646 (s), 592 (w), 553 (w), 503 (w), 482 (m), 464 (s), 410 (s).

Raman ($cm^{-1}$): 3125 (w), 2920 (w), 1572 (m), 1539 (w), 1455 (m), 1376 (s), 1301 (w), 1194 (s), 1174 (s), 1050 (s), 1003 (w), 851 (w), 818 (w), 780 (w), 757 (w), 729 (w), 596 (w), 513 (m), 500 (m), 374 (w), 221 (m), 170 (m).

Elemental analysis calcd for $C_{108}H_{136}B_4Co_4N_{42}Ru$: C 53.99, H 5.71, N 24.49; found: C 53.70, H 5.79, N 24.15.

ICP-OES Ru/Co ratio expected 1 : 4; measured 1 : 3.99.

$^1$H-NMR (400 MHz, $CDCl_3$): $\delta$ = 44.90 (s, 12H, $CH_{arom}$), 43.78 (s, 36H, $CH_3$), 42.08 (s, 12H, $CH_{arom}$), −13.73 (s, 36H, $CH_3$), −71.91 (s, 36H, $CH_3$).

**$[RuNi_4(Tp^*)_4(Me_2bta)_6]$ (5).** A solution of $[NBu_4][Tp^*]$ (160 mg, 0.30 mmol) in degassed DMF (1.5 mL) was added dropwise to a solution of **2** (100 mg, 0.03 mmol) in degassed DMF (1.0 mL) under argon atmosphere. The solution was stirred at rt for 2 h. The mixture was allowed to stand for 5 d, the participate was filtered and washed with methanol. The product was dissolved in trichloromethane and additionally filtered over a short column of basic aluminum oxide. Slow evaporation of the solvent yields **5** as a light brown crystalline product (145 mg, 0.06 mmol, 92%).

IR ($cm^{-1}$): 3347 (w), 3083 (w), 2965 (m), 2919 (s), 2857 (m), 2512 (m), 2335 (w), 1725 (w), 1544 (s), 1482 (m), 1444 (s), 1417, (s), 1375 (s), 1351 (s), 1305 (w), 1392 (m), 1259 (m), 1205 (s), 1184 (s), 1097 (m), 1060 (s), 1043 (s), 998 (s), 860 (s), 806 (s), 775 (s), 723 (m), 694 (8s), 6656 (m), 644 (s), 588 (w), 551 (w), 503 (w), 460 (m), 464 (s), 408 (s).

Raman ($cm^{-1}$): 3124 (w), 3078 (w), 2928 (m), 2730 (w), 1572 (m), 1542 (w), 1459 (s), 1377 (s), 1310 (w), 1200 (s), 1173 (s), 1058 (s), 1002 (w), 855 (w), 728 (w), 594 (w), 516 (m), 503 (s), 480 (w), 389 (w), 331 (w), 213 (m), 172 (w).

Elemental analysis calcd for $C_{108}H_{136}B_4Ni_4N_{42}Ru$: C 54.01, H 5.71, N 24.50; found: C 53.59, H 5.79, N 24.20.

ICP-OES Ru/Ni ratio expected 1 : 4; measured 1 : 3.94.

$^1$H-NMR (400 MHz, $CDCl_3$): $\delta$ = 47.35–46.47 (m, 12H, $CH_{arom}$), 29.86 (s, 6H, $CH_{arom}$), 0.12 (s, 36H, $CH_3$), −1.08 (s, 36H, $CH_3$), −2.92 (s, 6H, $CH_{arom}$), −8.83(s, 36H, $CH_3$).

**$RuZn_4(Me_2bta)_6(Tp^*)_4$ (6).** A solution of $[NBu_4][Tp^*]$ (80 mg, 0.15 mmol) in degassed DMF (1.5 mL) was added dropwise to a solution of $[RuZn_4Cl_4(Me_2bta)_6]$ (50 mg, 0.03 mmol) in degassed DMF (1.5 mL) under argon atmosphere. The solution was stirred at rt for 2 h. The mixture was allowed to stand for

1 d, the precipitate was filtered and washed with methanol. The product was dissolved in trichloromethane and additionally filtered over a short column of basic aluminum oxide. Slow evaporation of the solvent yields 6 as a yellow crystalline product (69 mg, 0.03 mmol, 87%).

IR ($cm^{-1}$): 3112 (w), 3075 (w), 2965 (m), 2925 (s), 2854 (m), 2730 (w), 2503 (m), 1733 (w), 1681 (m), 1571 (w), 1542 (s), 1486 (m), 1446 (s), 1413 (s), 1371 (s), 1348 (s), 1297 (m), 1292 (s), 1259 (m), 1203 (s), 1166 (s), 1064 (s), 1039 (s), 995 (s), 981 (s), 862 (s), 844 (s), 808 (s), 777 (s), 767 (s), 725 (w), 694 (s), 663 (s), 640 (s), 497 (w), 474 (s), 457 (s).

Raman ($cm^{-1}$): 3125 (w), 2925 (m), 2725 (w), 1572 (m), 1540 (w), 1457 (s), 1377 (s), 1307 (w), 1192 (s), 1168 (s), 1054 (s), 998 (w), 857 (w), 729 (m), 664 (w), 596 (m), 511 (m), 497 (s), 475 (w), 385 (w), 315 (w), 262 (w), 209 (w), 165 (m).

Elemental analysis calcd for $C_{108}H_{136}B_4Zn_4N_{42}Ru$: C 53.42, H 5.65, N 24.23; found: C 52.94, H 5.70, N 23.93.

ICP-OES Ru/Zn ratio expected 1 : 4; measured 1 : 4.07.

$^1$H-NMR (400 MHz, $CDCl_3$): $\delta$ = 5.76 (s, 12H, $CH_{arom}$), 5.30 (s, 12H, $CH_{arom}$), 2.57 (s, 36H, $CH_3$), 1.65 (s, 36H, $CH_3$), 0.13 (s, 36H, $CH_3$).

## Data availability

The data supporting the work presented in this manuscript are available in the ESI.†

The crystallographic data can be obtained from the Cambridge Crystallographic Data Centre as supplementary publication no. CCDC 2402422–2402426.†

## Conflicts of interest

There are no conflicts to declare.

## Acknowledgements

All authors are grateful to financial support from the University of Augsburg.

## References

1 J. K. McCusker, *Science*, 2019, **363**, 484.
2 A. Juris, V. Balzani, F. Barigelletti, S. Campagna, P. Belser and A. von Zelewsky, *Coord. Chem. Rev.*, 1988, **84**, 85.
3 D. G. Brown, N. Sanguantrakun, B. Schulze, U. S. Schubert and C. P. Berlinguette, *J. Am. Chem. Soc.*, 2012, **134**, 12354.
4 S. Lamansky, P. Djurovich, D. Murphy, F. Abdel-Razzaq, H. E. Lee, C. Adachi, P. E. Burrows, S. R. Forrest and M. E. Thompson, *J. Am. Chem. Soc.*, 2001, **123**, 4304.
5 C. Förster and K. Heinze, *Chem. Soc. Rev.*, 2020, **49**, 1057.
6 L. Conti, E. Macedi, C. Giorgi, B. Valtancoli and V. Fusi, *Coord. Chem. Rev.*, 2022, **469**, 214656.
7 C. Parella, A. Blanquer, S. Sinha, E. Hümpfner, J. Hernando, E. Mora, X. Fontrodona, Z. Kelemen, C. Nogués, R. Núñez, *et al.*, *Dyes Pigm.*, 2024, **224**, 111985.
8 C. K. Prier, D. A. Rankic and D. W. C. MacMillan, *Chem. Rev.*, 2013, **113**, 5322.
9 M. Parasram and V. Gevorgyan, *Chem. Soc. Rev.*, 2017, **46**, 6227.
10 D. W. Thompson, A. Ito and T. J. Meyer, *Pure Appl. Chem.*, 2013, **85**, 1257.
11 M. D. Kärkäs, E. V. Johnston, O. Verho and B. Akermark, *Acc. Chem. Res.*, 2014, **47**, 100.
12 Y. Chi and P.-T. Chou, *Chem. Soc. Rev.*, 2010, **39**, 638.
13 V. W.-W. Yam and K. M.-C. Wong, *Chem. Commun.*, 2011, **47**, 11579.
14 C. E. Welby, S. Grkinic, A. Zahid, B. S. Uppal, E. A. Gibson, C. R. Rice and P. I. P. Elliott, *Dalton Trans.*, 2012, **41**, 7637.
15 B. Happ, C. Friebe, A. Winter, M. D. Hager, R. Hoogenboom and U. S. Schubert, *Chem. – Asian J.*, 2009, **4**, 154.
16 J. T. Fletcher, B. J. Bumgarner, N. D. Engels and D. A. Skoglund, *Organometallics*, 2008, **27**, 5430.
17 R. C. Rocha and H. E. Toma, *Transition Met. Chem.*, 2003, **28**, 43.
18 P. A. Scattergood and P. I. P. Elliott, *Dalton Trans.*, 2017, **46**, 16343.
19 R. H. Laye, Q. Wei, P. V. Mason, M. Shanmugam, S. J. Teat, E. K. Brechin, D. Collison and E. J. L. McInnes, *J. Am. Chem. Soc.*, 2006, **128**, 9020.
20 D. Wang, J. Peng, H. Pang, P. Zhang, X. Wang, M. Zhu, Y. Chen, M. Liu and C. Meng, *Inorg. Chim. Acta*, 2011, **379**, 90.
21 S. Komeda, Y. In, K. Tomoo, K. Minoura, T. Sato, J. Reedijk, T. Ishida and M. Chikuma, *Inorg. Chim. Acta*, 2019, **495**, 118999.
22 S. Biswas, M. Tonigold, M. Speldrich, P. Kögerler, M. Weil and D. Volkmer, *Inorg. Chem.*, 2010, **49**, 7424.
23 T. W. Werner, S. Reschke, H. Bunzen, H.-A. K. von Nidda, J. Deisenhofer, A. Loidl and D. Volkmer, *Inorg. Chem.*, 2016, **55**, 1053.
24 K. Knippen, D. Matuszczyk, M. Kraft, B. Bredenkötter, G. Eickerling, T. Lis, D. Volkmer and M. Stępień, *Chem. – Eur. J.*, 2022, **28**, e202103480.
25 C. Kuratowski, *Fund. Math.*, 1930, **15**, 271.
26 Y.-Y. Liu, M. Grzywa, M. Tonigold, G. Sastre, T. Schüttrigkeit, N. S. Leeson and D. Volkmer, *Dalton Trans.*, 2011, **40**, 5926.
27 (*a*) D. Denysenko, M. Grzywa, M. Tonigold, B. Streppel, I. Krkljus, M. Hirscher, E. Mugnaioli, U. Kolb, J. Hanss and D. Volkmer, *Chemistry*, 2011, **17**, 1837; (*b*) D. Denysenko, M. Grzywa, J. Jelic, K. Reuter and D. Volkmer, *Angew. Chem., Int. Ed.*, 2014, **53**, 5832.
28 D. Hayes, L. Kohler, R. G. Hadt, X. Zhang, C. Liu, K. L. Mulfort and L. X. Chen, *Chem. Sci.*, 2018, **9**, 860.
29 W. G. Daul, M. Hirrle, B. Eisfeld, M. Kraft, H.-A. K. von Nidda and D. Volkmer, *Inorg. Chem.*, 2024, **63**, 5027.

30 R. Röß-Ohlenroth, C. Freudig, M. Kraft, H. Bunzen and D. Volkmer, *Cryst. Growth Des.*, 2022, **22**, 379.
31 (*a*) I. Solomon, *Phys. Rev.*, 1955, **99**, 559; (*b*) J. L. Battiste and G. Wagner, *Biochemistry*, 2000, **39**, 5355.
32 L. Yang, D. R. Powell and R. P. Houser, *Dalton Trans.*, 2007, 955.
33 D. W. C. MacMillan, T. P. Yoon and C. R. J. Stephenson, *Visible Light Photocatalysis in Organic Chemistry*, Wiley-VCH Verlag GmBH, 2018.
34 J. Vachon, M. Mayoral, D. Ayme-Perrot and S. B. Schougaard, *ECS Trans.*, 2009, **19**, 113.
35 D. C. L. de Alwis and F. A. Schultz, *Inorg. Chem.*, 2003, **42**, 3616.
36 T. F. S. Silva, L. M. Martins, M. F. C. Da Guedes Silva, A. R. Fernandes, A. Silva, P. M. Borralho, S. Santos, C. M. P. Rodrigues and A. J. L. Pombeiro, *Dalton Trans.*, 2012, **41**, 12888.
37 M. Felici, P. Contreras-Carballada, Y. Vida, J. M. M. Smits, R. J. M. Nolte, L. de Cola, R. M. Williams and M. C. Feiters, *Chemistry*, 2009, **15**, 13124.
38 K. Kalyanasundaram, *Coord. Chem. Rev.*, 1982, **46**, 159.
39 A. B. P. Lever, *Inorganic Electronic Spectroscopy*, Elsevier Publishing Company, Amsterdam, 1968.
40 A. C. G. Hotze, J. A. Faiz, N. Mourtzis, G. I. Pascu, P. R. A. Webber, G. J. Clarkson, K. Yannakopoulou, Z. Pikramenou and M. J. Hannon, *Dalton Trans.*, 2006, 3025.
41 R. L. Lord, M. M. Allard, R. A. Thomas, O. S. Odongo, H. B. Schlegel, Y.-J. Chen and J. F. Endicott, *Inorg. Chem.*, 2013, **52**, 1185.
42 L. Krause, R. Herbst-Irmer, G. M. Sheldrick and D. Stalke, *J. Appl. Crystallogr.*, 2015, **48**, 3.
43 G. M. Sheldrick, *Acta Crystallogr., Sect. A*, 2015, **71**, 3.
44 G. M. Sheldrick, *Acta Crystallogr., Sect. C*, 2015, **71**, 3.